Pergamon

1359-6454(95)00448-3

Acta mater. Vol. 44, No. 9, pp. 3643–3654, 1996

Published by Elsevier Science Ltd

1359-6454/96 $15.00 + 0.00

DIRECT OBSERVATION OF SOLIDIFICATION MICROSTRUCTURES AROUND ABSOLUTE STABILITY

A. LUDWIG† and W. KURZ

Department of Materials, Swiss Federal Institute of Technology Lausanne (EPFL), CH-1015 Lausanne, Switzerland

(Received 16 August 1995; in revised form 30 November 1995)

Abstract—This paper presents, for the first time, experimental evidence for absolute stability in a transparent alloy. The succinonitrile–argon system was used to investigate the morphological transition from a cellular to a planar solid–liquid interface at high solidification velocities. Directional solidification of the organic contained in thin capillary tubes was observed *in situ* with an optical microscope. At the maximum interface velocity of 1.5 mm/s, a reduction of the solute content of the alloy resulted in a morphological transition from a cellular to a planar growth front. This transition developed in three stages: (i) transition from deep cylindrical cells to mixed patterns of cylindrical and elongated cells; (ii) transition from cylindrical and elongated cells to low amplitude cells; (iii) transition from low amplitude cells to plane front. Within the limits of uncertainties with respect to the material properties and the thermal gradient, correspondence between the experimental results on plane front transition and linear stability theory exists. It is shown that the transitions observed are located in the region near the limit point of the neutral stability curve on the branch for absolute morphological stability. *Copyright © 1996 Acta Metallurgica Inc.*

1. INTRODUCTION

During directional solidification of alloys, the microstructures which form depend on the alloy composition, C_0, and the process parameters: temperature gradient, G, and solidification velocity, V. At the origin of any solidification microstructure is the development of morphological instabilities of a smooth (stable) crystal melt interface [1]. Under conditions of directional solidification ($G > 0$) the stable solid–liquid interface is planar. Above a critical velocity, V_C, the plane front breaks down to form cellular patterns. Further increase of V results in the development of dendritic microstructures and finally, at very high rates, in a reverse transition from dendrites to cells and finally to plane front [2]. This restabilisation of the plane front has been predicted by linear stability analysis of Mullins and Sekerka (MS) already in 1964 [3] and is called absolute stability. The corresponding velocity is known as the limit of absolute stability, V_{abs}. A range of perturbation wavelengths is obtained (Fig. 1) for a given growth rate between V_C and V_{abs}. The range of wavelengths is limited; at the upper bound by diffusion and at the lower side by capillary forces.

The original MS analysis, which was based on the assumption of local equilibrium, has been extended in several ways. In their general expression Coriell and Sekerka [4] considered the solute distribution coefficient, k, to be a function of velocity, concentration and temperature, and introduced attachment kinetic effects. This led to the prediction that, at high velocities where non-equilibrium phenomena at the solid–liquid interface become important, the interface may not only be morphologically unstable but may also display oscillatory instabilities.

Parallel to this, the velocity dependence on the distribution coefficient has been derived by Aziz [5] and non-equilibrium effects were presented in a thermodynamically consistent way by Boettinger and Coriell [6, 7] following the original work by Baker and Cahn [8]. Davis *et al.* [9–12] subsequently studied the various branches of morphological and oscillatory instabilities when non-equilibrium conditions prevail at the interface. They compared their results with experimental observations on banded structures near the limit of absolute stability and found a reasonable degree of correspondence between experiment and theory. In allowing the interface to develop large amplitude perturbations, Karma and Sarkissian were able to further explore the oscillating interface response (banding) in more detail [13, 14]. For a more complete discussion of this subject, the reader is referred to Refs [14, 15].

In order to gain a better insight into these microstructural transitions close to V_{abs}, which are relevant to rapid solidification, direct observations would be very valuable. Due to the opaque nature of metals, only indirect observations can be made

†Present address: Gießerei-Institut, Rheinisch-Westfälische Technische Hochschule Aachen, D-52056 Aachen, Germany.

however. Several transparent organic alloys have been used in the past for modelling the solidification behaviour of metals. These are the so-called plastic crystals, organic substances with a low melting temperature and a low melting entropy [16].

Only very few experiments have been undertaken which aimed for the direct *in situ* observation of the microstructural transitions around the limit of absolute stability. Trivedi *et al.* [17] investigated the solidification microstructures in the transparent carbon–tetrabromide system at high velocities within thin cells. These authors observed the transition from a dendritic to a micro-cellular morphology when the interface was accelerated. However, they could not reach sufficient high velocities to observe, in their alloys, a restabilization of the plane front.

The aim of the present work was therefore to reach steady state growth conditions which would make it possible to directly observe the solid–liquid interface close to absolute stability and to make quantitative comparisons between the measurements and predictions of stability theory.

2. EXPERIMENTAL PROCEDURE

The succinonitrile (SCN)–argon system has been chosen for its well-characterised thermophysical properties [18, 19] and its low melting point which allows observation of the phenomena under the optical microscope.

2.1. *Solidification experiments*

The apparatus for rapid solidification of the organics is shown in Fig. 2. A 900 mm long borosilicate glass capillary with a square cross section, an inner opening of 200 μm and a wall thickness of 100 μm containing the alloy was placed inside a heating and cooling device. The hot zone was formed by a 900 mm long tube heated by water. The cold zone consisted of a 70 mm long chamber, where

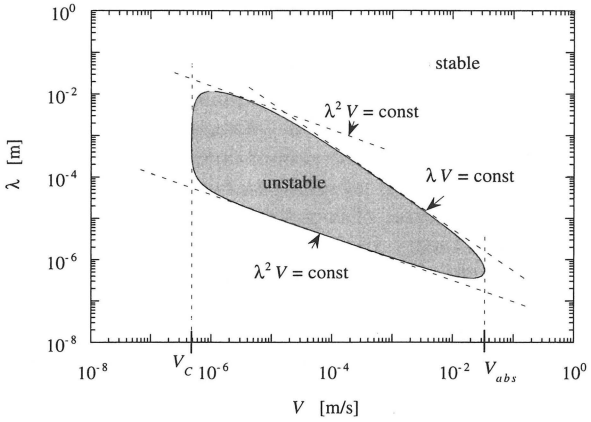

Fig. 1. Window of unstable solidification front in the λ–V-plane due to linear stability analysis for DS of SCN–Ar ($\Delta T_0 = 1$K and $G_L = 500$K/m). The constitutional undercooling criterion bounds the region by a vertical line at V_C while absolute stability is reached at V_{abs}.

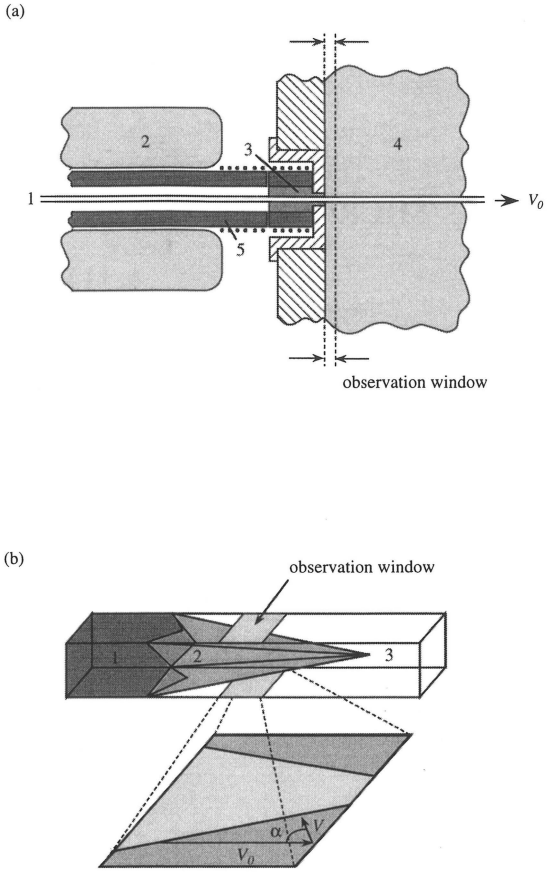

Fig. 2. (a) Details of the experimental arrangement (schematic): (1) capillary tube, (2) heater (warm water), (3) silicon seal, (4) chamber with liquid coolant, (5) copper tube with heatable seal region. (b) Upper part: 3D-view of the principle shape of the solid–liquid interface within the capillary: the first solid appeared as surface dendrites in the edges of the tube. Lower part: 2D-projection of the solid–liquid interface seen from a typical observation window. The relationship between pulling speed, V_0 and local growth rate, V, is $V = V_0 \cdot \cos\alpha$.

the liquid coolant was pumped through. The capillary tube was in direct contact with the coolant. The entrance and exit holes were blocked with silicon rubber seals. To avoid solidification taking place within the seal, this region was heated by an additional heater [Fig. 2(a)]. As a result, most of the solidification process took place inside the coolant, just behind the entrance seal. The pulling speed of the capillary, V_0, was varied from 1 to 30 mm/s. The solidification inside the tube was observed with the aid of an optical microscope and recorded with a video system. A sensitive S-VHF camera with an exposure time of 100 μs was used in combination with a Xe-lamp as the light source. The image frequency was 50 Hz.

Under the experimental conditions used, the solidification front was nearly parallel to the side walls of the capillary leading to the solid–liquid interface of pyramidal geometry as shown schemati-

cally in Fig. 2b. Thanks to the square section of the tube, the solid–liquid interface could be observed from the top as well as from the side. Figure 3 shows a typical image of a cellular interface. The microscope was focused on the lower interface. Although the depth of focus was limited, the cellular morphology is also visible at the side walls. The distance between two opposite solidification fronts was approximately 100 μm (corresponding to 50 μm solid layer on each side), which was characteristic for the observation window used in the experiments presented below. The actual growth rate was obtained from the angle α between the interface normal and the pulling direction, by: $V = V_0 \cdot \cos\alpha$ where V_0 is the pulling velocity [Figs 2(b) and 3].

To obtain an average value of α, five different images in direct chronological order were evaluated. Measuring errors were minimised by measuring and averaging the angles of the two opposite interfaces from the same image. This procedure was carried out twice for each angle. A main average value was calculated from the angles of the five images. The standard deviation of this averaging was taken as the measuring error for α.

Several experimental runs were performed to investigate the influence of the different process parameters on V. The initial melt temperature, T_H, the temperature at the entrance seal, T_G, and the pulling speed, V_0, could be varied within a wide range without changing V. All the experiments presented in this paper were performed with $T_H = 331.2$ K and $332 \leqslant T_G \leqslant 334$ K. The cooling temperature T_C was the only quantity by which the solidification rate could be clearly influenced. Water was used as a coolant for the temperature range $275 \leqslant T_C \leqslant 328$ K and alcohol for $253 \leqslant T_C \leqslant 275$ K. Depending on the temperature of the coolant used, the resulting solidification velocity varied between $V = 0.3$ and 1.5 mm/s for $V_0 = 4.5$ and 11 mm/s, respectively.

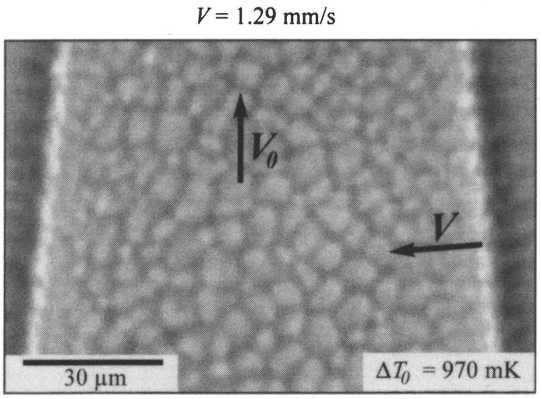

Fig. 3. Cellular interface morphology of a SCN–Ar alloy with $\Delta T_0 = 970$mK. The liquid–solid interface possessed pyramidal geometry with four flat sides. The microscope was focused on the lower interface. The local solidification velocity, calculated from the slopes of the side faces, was $V = 1.29$mm/s.

Table 1. Estimated solidus–liquidus interval ΔT_0 with the corresponding measuring error and the related Ar concentration C_0 for the alloys used in this work. C_0 has been calculated with the material properties given in Appendix B

ΔT_0 (mK)	Error (mK)	C_0 (wt%)
970	±70	0.0516
700	±60	0.0372
570	±50	0.0299
415	±40	0.0221
280	±40	0.0149
235	±40	0.0125
60	±40	0.0032

2.2. *Purification of SCN*

Succinonitrile was distilled under vacuum and then zone-refined with more than 50 passes. The purified part of the zone-refined material was then used to fill the capillary tubes. The purified SCN within the tubes had a solidus–liquidus temperature interval of about 60 mK. Further details of the distillation and zone-refining can be found in Ref. [20].

2.3. *Filling of the capillary tubes*

The filling apparatus consisted of a long water-heated quartz tube connected to the flask which was filled with the purified succinonitrile. The other end of the quartz tube was tightly sealed with a silicon disc. The capillary was threaded through a small hole in the centre of this disc, so that most of the capillary was located inside the quartz tube. The filling apparatus as well as the free end of the capillary tube was connected to a vacuum system. To avoid contamination of the SCN stock, capillary tubes were only inserted or removed, under a small over pressure of argon when the SCN stock was solidified. Because of the difficulties of cleaning and drying the capillary tubes, they were used as delivered from the manufacturer. Further details of the filling procedure can be found in Ref. [20a].

2.4. *Determination of T_L and T_S of the alloy within the capillary tubes*

Instead of concentration, the more convenient equilibrium solidus–liquidus interval $\Delta T_0 (= T_L - T_S)$ was used for the characterisation of the various alloys. The solidus and liquidus temperatures (T_S and T_L) were measured by heating a 75 mm long section of the tube and investigating the melting and solidification process under the microscope. In order to achieve homogeneous temperature distribution, a heated water jacket was placed around this part. The temperature in the centre of the cooling jacket was measured with a quartz thermometer. The thermostat for heating the water had the same relative accuracy as the quartz thermometer (±5 mK), the temperature within the jacket varied by some ±15 mK. Thus, the relative accuracy of the entire system was estimated to be about ±20 mK. The estimated solidus–liquidus interval ΔT_0 of the alloys used in this work with the corresponding measuring error and the related Ar concentration C_0 are given in Table 1.

Because of the dependence of T_S and T_L on the pressure, it had to be ensured that a cavity large enough for the expansion due to melting was present within the section of interest. Therefore, the SCN was melted at the end of the capillary tube where a cavity was present and then the molten zone was moved towards the section of interest. Further details can be found in Refs [18, 20a].

3. RESULTS

At high pulling velocities, the liquid pool was very long and the solidification front was nearly parallel to the side walls. The first solid was formed within the edges, as surface dendrites. After impingement of the four surface dendrites from the edges, the solid–liquid interface revealed a pyramidal geometry [Fig. 2(b)]. With the exception of the beginning and end of the solidification region, the solid–liquid interface was macroscopically flat and therefore the growth velocity was constant over most of the half-width of the capillary.

Figure 4 shows the morphological transitions of the solid–liquid interface with four different argon concentrations. Four different interface morphologies could be distinguished:

(i) for alloys with $\Delta T_0 \geqslant 415$ mK, cylindrical cells [Fig. 4(a)];
(ii) at $\Delta T_0 = 280$ mK elongated (lamellar) and cylindrical cells [Fig. 4(b)];
(iii) for $\Delta T_0 = 235$ mK coarse grains with a substructure of low amplitude perturbations [Fig. 4(c)];
(iv) at $\Delta T_0 = 60$ mK only coarse grains which revealed no perturbations† [Fig. 4(d)].

The velocity dependence of the interface morphology, where a mixture of cylindrical and elongated (lamellar) cells were present [$\Delta T_0 = 280$ mK, Fig. 4(b)], is shown in Fig. 5. It can be seen that the size of the structure decreased with increasing velocity. For one solidification velocity, the width of the elongated cells was comparable to the diameter of the cylindrical cells. The relative amount of elongated cells increased with increasing velocity. Relatively large areas with irregular curved boundaries were present [see the arrows in Figs 5(a) and (e)] at both low and high velocities.

The orientation of the elongated cells varied slightly during one experiment. The elongated cells were usually aligned approximately in the pulling direction with only small deviations of less than 15°. Only in a few cases did the orientation of the elongated cells differ clearly from the pulling direction, sometimes by even as much as 90°.

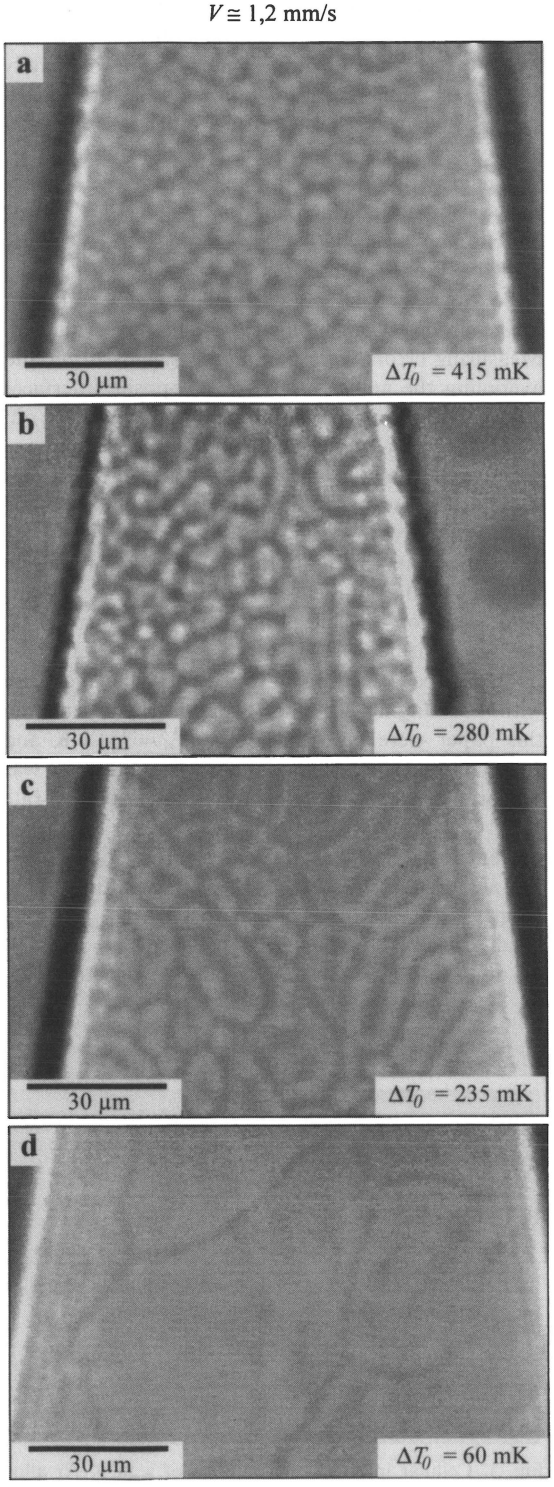

Fig. 4. Transition from a cellular interface (a) to a grain-like planar interface (d) by reducing the Ar concentration for $V \approx 1.2$mm/s: (a)$\Delta T_0 = 415$mK, (b) $\Delta T_0 = 280$mK, (c) $\Delta T_0 = 235$mK, (d) $\Delta T_0 = 60$mK.

†The shadowing of substructures, which represent low amplitude perturbations has topological similarity with the grains, in which they were found. An unsharp shadowing crossing a grain boundary, like in the grains shown in Figs 4(d) and 6(a), is thus assumed to originate from the grain boundaries from the opposite interface, which was out of focus.

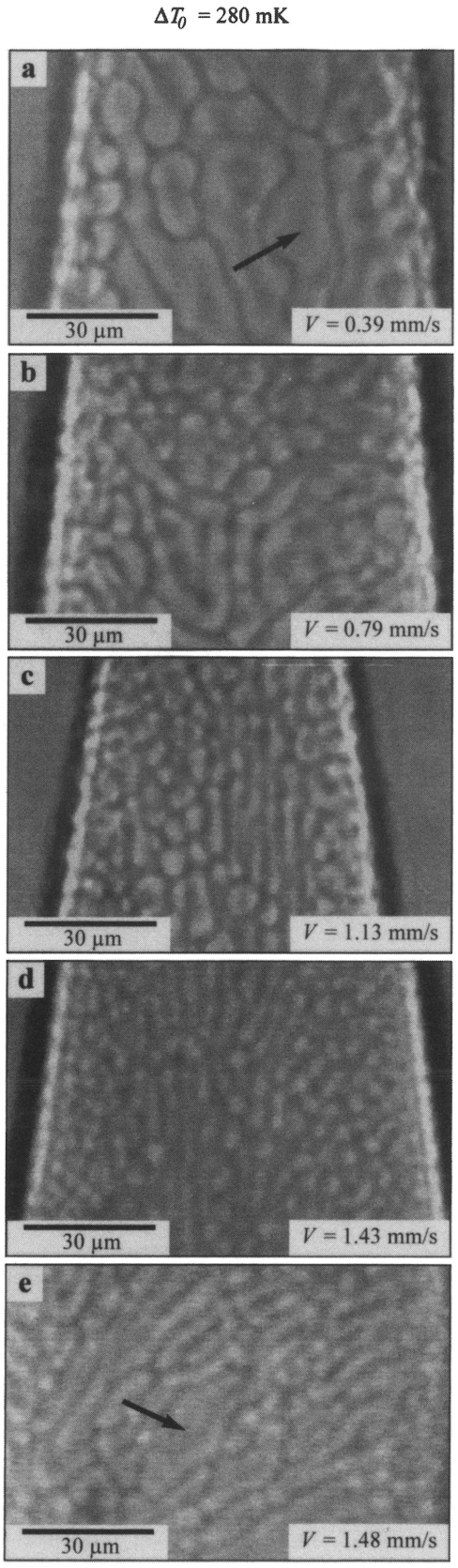

Fig. 5. Velocity dependence of the interface morphology of the alloy, $\Delta T_0 = 280$ mK: (a) $V = 0.39$ mm/s, (b) $V = 0.79$ mm/s, (c) $V = 1.13$ mm/s, (d) $V = 1.43$ mm/s, (e) $V = 1.48$ mm/s.

Figure 6 shows the velocity dependence of the interface morphology for $\Delta T_0 = 235$ mK. At low velocity, the grain-like structure revealed no substructure [Fig. 6(a)]†. At $V \geqslant 0.78$ mm/s [Figs 6(b)–(e)], the grain-like structure had a substructure which revealed curved and ring-shaped configurations. The substructure was most pronounced at $V = 1.04$ and 1.34 mm/s [Figs 6(c) and (d)]. At higher solidification velocities, the perturbation seemed to disappear again [Fig. 6(e)].

The size of the substructure as indicated in Fig. 6(c) was estimated to be of the order of $\lambda = 4.7$ μm for $V = 1.04$ mm/s. Due to the large error in measuring λ, a quantitative evaluation of the $\lambda - V$ dependence was not possible.

In order to understand the origin of the grain structure, the initial stage of solidification generally present within the edges of the tubes was observed in more detail. To do this, the temperature of the coolant had to be increased to $T_C = 328$ K. The tube was turned by 20° about its axis to permit observation of the very first solidification in the edge. Figure 7(a) shows the tip region of the solid–liquid interface in the edge which is in the form of a surface dendrite ($\Delta T_0 = 60$ mK). [The light vertical stripe in image (a) was due to the optical effect of the tube edge.] The interface was formed by a dense array of secondary branches behind the tip of the surface dendrite. The impingement of two surface dendrites from neighbouring edges is shown in Fig. 7(b). The thickness of the solid layer at this stage is still of the order of a few microns. The further evolution of the interface is illustrated in Figs 7(c)–(f) and showed that the parallel boundaries between the cell-shaped branches changed with time into a more polygonal configuration [Fig. 7(f)] and approached the grain structure of Fig. 4(d).

4. DISCUSSION

In order to interpret the results a closer look at the neutral morphological stability curve is needed. This curve specifies the growth conditions of an interface at the limit of stability, for example as a function of growth rate and composition (or ΔT_0) for a given alloy system and temperature gradient. The neutral stability curve in the $V - \Delta T_0$-plane was calculated for the present system using the Huntley and Davis model [12]. Their equation (4.2) is complex. However, since only steady-state solutions are concerned, it can be transformed into a simpler expression which is widely used in metallurgy [2, 21] (see Appendix A). Such diagrams are shown in Fig. 8 for SCN–argon. These curves show the existence of a critical composition, C_0^* (or ΔT_0^*), below which the interface is morphologically stable at all solidification velocities. To the right of the curves, the solid–liquid interface is morphologically unstable. The lower branch of the

See footnote on the preceding page.

neutral stability curve asymptotically reaches the limit of constitutional undercooling, while the upper branch tends towards a straight line representing absolute stability. The neutral stability curve for oscillatory instabilities is not shown in this figure. It looks similar to the morphological stability curve but is found at higher velocities [12].

Some of the thermophysical properties of the SCN–Ar system, as well as the temperature gradient are not well known. Therefore, a sensitivity analysis of the influence of the variation of these parameters on the resulting stability limit has been undertaken.

The material properties used for the calculations are given in Appendix B. The most important and somewhat uncertain quantities are the equilibrium distribution coefficient k, the diffusion coefficient D and the rate of diffusion through the interface (given by the ratio of the coefficient for diffusion across the solid–liquid interface and the interface width a_0). A detailed evaluation of the values chosen is given in Appendix B.

The interfacial temperature gradient in the liquid, G_L, for steady-state plane front growth (at T_S) was approximated by assuming that the temperature in the centre of the tube is still the same as the temperature of the heater when the thickness of the solidified layer is of the order of 50 μm and that the temperature profile in front of the interface is linear. This leads to a lower bound estimate of $G_L \sim 2 \times 10^3$ K/m ($\Delta T_0 = 60$ mK) and $G_L \sim 9 \times 10^3$ K/m ($\Delta T_0 = 415$ mK). If G_L in front of the solid–liquid interface is not constant (due to convection or unsteady thermal diffusion), its value may be several times larger.

Figures 8(a)–(d) show the influence of G_L, D, k and a_0 on the neutral stability curve for SCN–Ar. G_L mainly changes the lower boundary of the stability curve [Fig. 8(a)], k and a_0 mainly the upper boundary [Fig. 8(c) and (d)] and D affects both the lower and upper boundaries [Fig. 8(b)]. Increased a_0 only affects the upper boundary indirectly by allowing k to increase faster at high velocities. This non-equilibrium effect is only to be considered for $V \geqslant 2 \times 10^{-3}$ m/s [Fig. 8(d)] which is beyond the maximum V of the present experiments.

Before the experimental results are compared with the theory, some further remarks have to be made. The characteristic scale of the microstructure was 1 10–40 times smaller than the thickness of the solidified layer. Due to the flat faces of the pyramidal solid–liquid interface, the growth velocity can be regarded as constant and solidification as steady state. The characteristic diffusion distance for

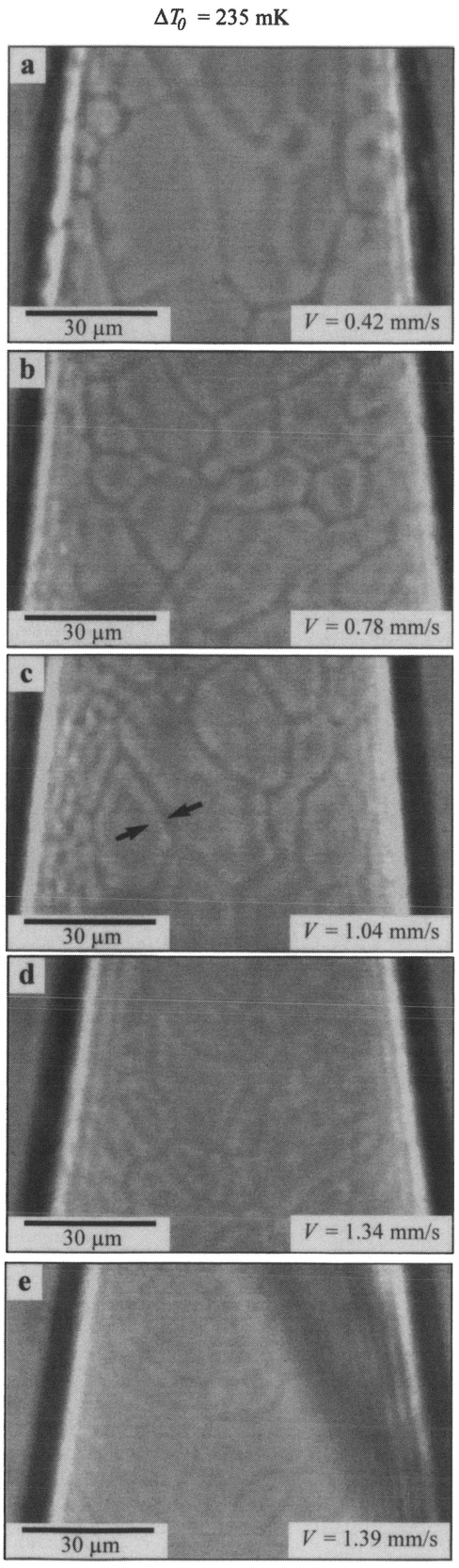

Fig. 6. Velocity dependence of the interface morphology of the alloy, $\Delta T_0 = 235$mK, which revealed a grain structure with a low amplitude substructure: (a) $V = 0.42$mm/s, (b) $V = 0.78$mm/s, (c) $V = 1.04$mm/s, (d) $V = 1.34$mm/s, (e) $V = 1.39$mm/s. (The dark band in this figure was caused by an object outside the capillary tube.)

Fig. 6.

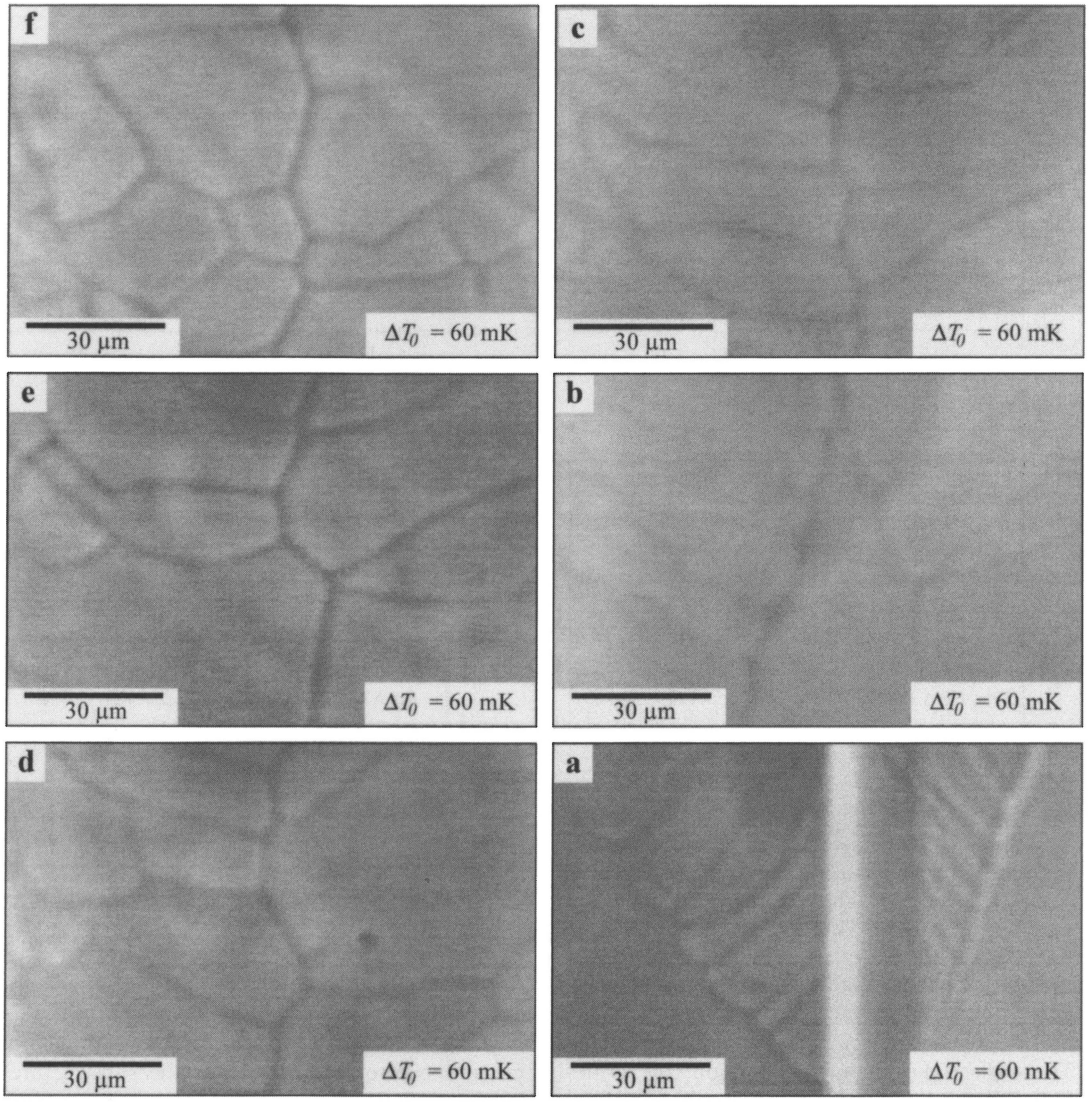

Fig. 7. The origin of the grain-like solidification morphology of the alloy, $\Delta T_0 = 60$mK. First solid to form as surface dendrite within the edges of a tube (a). Impingement of two neighbouring surface dendrites (b). Further evolution of the interface (c)–(f). The parallel boundaries transformed into more circular configurations (f).

the solidification velocities employed, D/V, is of the order of several micrometers. Thus, overlapping of the solute diffusion boundary layers from opposite solid–liquid interfaces does not take place.

The experimental results are summarised in a V–ΔT_0-diagram where four different types of markers were used to indicate the morphological changes (Fig. 9). For k and a_0 as given in Appendix B and $G_L = 5 \times 10^4$ K/m† and $D = 6 \times 10^{-10}$ m^2/s, the neutral stability curve correlates well with the experimental observations, if the following assumptions are made: (1) the grain structure without a substructure represents the plant front [Fig. 4(d)]; (2) the substructure in the grains (Fig. 6) represents shallow perturbations growing just above the stability threshold.

The first assumption can be justified by the fact that (i) the material with the highest purity (60 mK), which according to theory is definitely within the stable region, shows the same grain structure; (ii) the grain structure is formed very early in the process. The branches of the surface dendrite, which are only a few microns thick when they collide, transform during further growth into mosaic-like configurations [Fig. 7(f)]. This transformation process is not yet completely understood. It may be that the grains are the product of recrystallisation, as stresses which

†This temperature gradient has been used to fit the theoretical curve to the experimental results. Its value seems to be acceptable in view of the discussion on G_L pursued above.

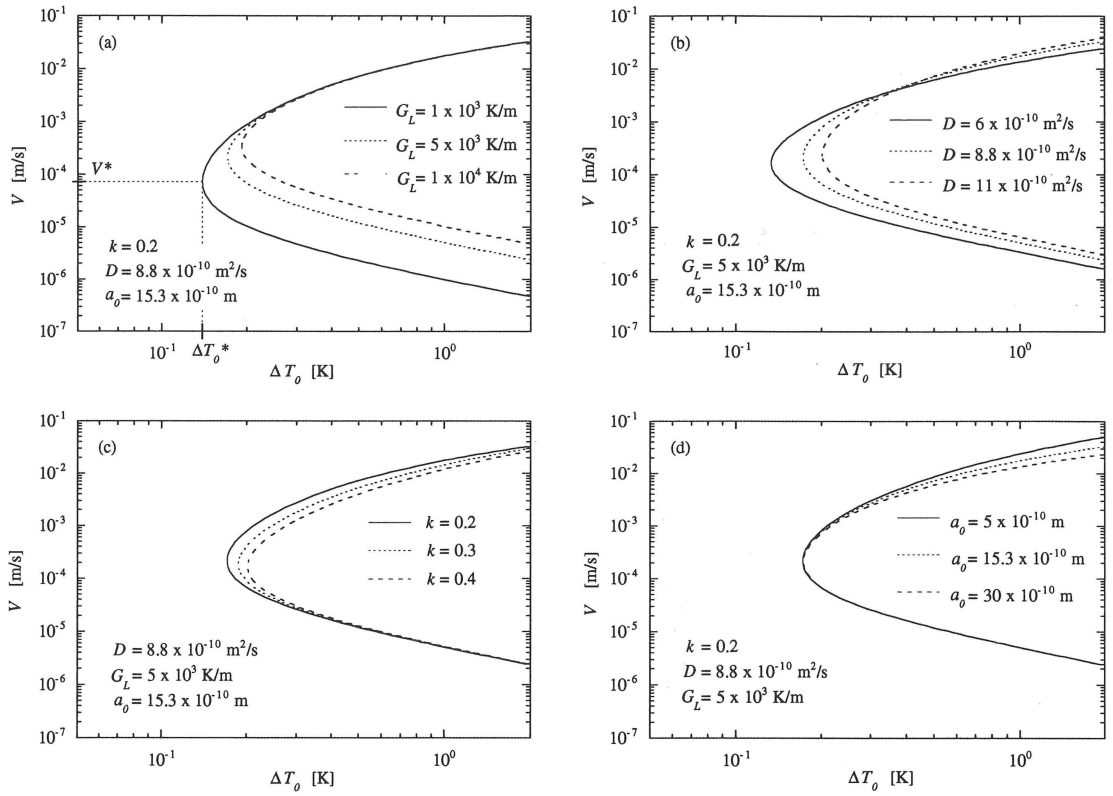

Fig. 8. Parameter study of the neutral stability curve for the SCN–Ar-system according to the linear stability analysis of Huntley and Davis [12] in the V–ΔT_0-plan. On the right hand side of this curve the planar growth front is morphologically unstable. G_L only changes the lower boundary of the stability curve (a), k and a_0 only the upper boundary [(c) and (d)] and D effects the lower and the upper boundary (b). Non-equilibrium effects have to be considered for $V \geqslant 2 \times 10^{-3}$m/s (d).

are high enough to multiply dislocations build up during cooling at the interface between SCN and glass.

To confirm the second assumption, the critical wavelength λ calculated for the onset of instability is compared with the size of the substructure measured from Fig. 6(c). Figure 10 shows the λ–ΔT_0-diagram calculated from linear stability theory for the same set of G_L, D, k and a_0 as in Fig. 9. Although the measuring error of the size of the substructure is large, correlation is satisfactory. (Note that the upper and lower branch correspond to low and high velocities, respectively.)

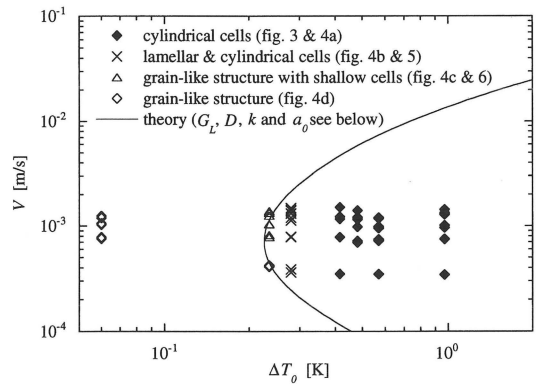

Fig. 9. For $G_L = 5 \times 10^4$K/m, $D = 6 \times 10^{-8}$m²/s, $k = 0.2$ and $a_0 = 15.3 \times 10^{-10}$m the neutral stability curve correlated well with the experimental observations. Note that the measuring error for ΔT_0 has to be assumed to be equal to or greater than $\pm$40mK (see Table 1). The measuring error for V is smaller than $\pm$0.07mm/s.

Voorhees *et al.* [22] and Ungar *et al.* [23] investigated the effect of grain boundaries on the stability of a planar solid–liquid interface at low velocities. They found that the threshold is shifted to somewhat lower values. Therefore, due to the grain structure of the planar front presented in this paper, instability is enhanced in our experiments. However, it goes beyond the scope of this work to discuss this effect quantitatively.

Another effect which has to be considered is convection. The shrinkage due to solidification, $\Delta\rho/\rho$, which for SCN is about 0.048, induces a flow within the capillary tube. Considering mass conservation, the average flow speed is given by $U = (\Delta\rho/\rho)V_0$. With V_0 of the order of 20 mm/s, a flow of about 1 mm/s can be estimated for these experiments, which is of the same order of magnitude as the solidification velocities. This convection is supposed to be laminar with a parabolic flow field along the tube axis.

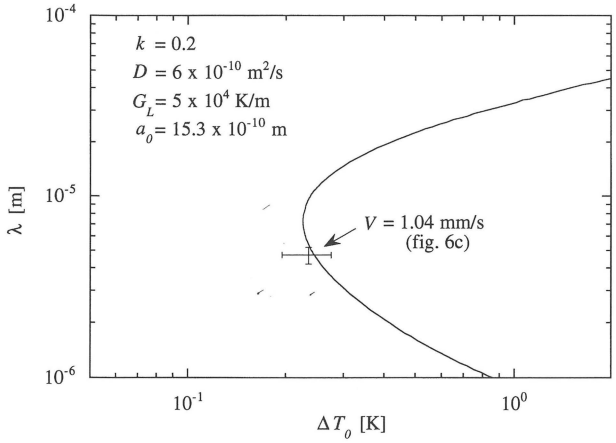

Fig. 10. Critical wavelength λ as a function of ΔT_0 for the same parameters as indicated in Fig. 9. The experimental value measured from Fig. 6(c) is also given. The corresponding solidification velocity is $V = 1.34$mm/s. Note that the lower branch corresponds to absolute stability and the upper to the limit of constitutional undercooling.

In order to discuss the influence of this flow on the stability of the planar solid–liquid interface in the present situation, the flow field near the interface must be distinguished from the flow field at the centre of the tube. The flow near the interface has a normal component, whereas the flow in the centre of the tube acts as a forced flow approximately parallel to the interface. As discussed by Davis [24] the flow normal to the interface shifts the whole neutral stability curve to a smaller V. According to Davis, this effect is of minor importance if $\Delta\rho/\rho$ is small.

The influence of a forced flow, parallel to the solid–liquid interface, on the morphological stability has been studied theoretically by several authors [25–28]. Coriell *et al.* [25] and Forth and Wheeler [26] examined two-dimensional disturbances which were periodic in flow direction and found that the flow stabilised the interface. However, if longitudinal-roll disturbances are considered, the flow decouples from the stability problem. Thus, the flow "selects" the longitudinal-roll disturbances. This might explain the preferred orientation of the elongated cells in axial direction, although, as mentioned above, the orientation was sometimes found to be perpendicular to pulling direction.

Hobbs and Metzener [27, 28] have examined the effect of a parallel forced flow on the interface near the absolute stability boundary. They found that, far from the nose of the neutral stability curve, the flow destabilises the interfaces at V_{abs}. It can be assumed that this effect is beyond the experimental range of this work [29]. After all, flow will have a certain effect on the transitions. A quantitative evaluation of this effect is, however, beyond the scope of this paper.

The question whether the morphological transitions observed near the limit point (C_0^*, V^*) are a super- or subcritical bifurcation cannot be answered by these experimental results. However, there are two indications which tend to suggest that both morphological transitions observed at low and high velocity are supercritical:

(i) Slight fluctuations in the angle between the interface normal and the axis of the tube, α, resulted in a small variation in V of a few percent. If the bifurcation is assumed to be subcritical, a small fluctuation of V near the threshold of stability would lead to a sudden change in the interface morphology. Because of the hysteresical nature of a subcritical bifurcation, this sudden change in the morphology would remain, even if V increased again over the threshold (within a certain limit). Such a change in the solidification pattern was not observed. For the $\Delta T_0 = 235$ mK alloy, the experiments were indeed performed near the threshold. This can be seen in Figs 6(a) and (b). For $V = 0.42$ mm/s [Fig. 6(a)] no substructure was found, whereas for $V = 0.78$ mm/s [Fig. 6(b)] a weak substructure could be seen, indicating the appearance of shallow cells.

(ii) As shown by Merchant and Davis, the transition point (TP) separating the subcritical from the supercritical branch of the neutral stability curve is about $C_0 \approx 0.1$ wt% for the SCN–acetone system [9]. Because of the similar material properties of the system used in this study with respect to SCN–acetone, it can be assumed that TP in the SCN–Ar system is of the same order of magnitude. The transition from elongated to shallow cells appeared at a concentration of the order of $C_0 \approx 0.01$ wt% ($\Delta T_0 \approx 200$ mK see Table 1), which is noticeably smaller than C_0 for TP in the SCN–acetone system.

No oscillations of the solid–liquid interface have been observed. This may be explained in the following way: Fig. 8(d) shows that non-equilibrium effects only become important at velocities which are larger than the maximum value attainable in these experiments. As the driving force behind the

oscillations at high velocities is essentially given by the variation of the distribution coefficient with velocity, dk/dV, and this variation is very small at 1–2 mm/s, banding is not expected.

5. SUMMARY

The first direct evidence is presented for a transition from cellular to plane front solidification with increasing interface velocity in SCN–argon alloys which solidify like metals. The *in situ* observations have been made under conditions of absolute stability close to the nose of the neutral stability curve in V–C_0 space. Several interesting transition patterns have been observed which are summarized as follows.

(1) Reducing the solute content of a binary alloy results in a morphological transition from deep cylindrical cells to a planar growth front. This transition goes through three different stages: (i) transition from cylindrical cells to a pattern where elongated and cylindrical cells coexist; (ii) transition from the elongated and cylindrical cells to shallow (low amplitude) perturbations; (iii) transition from the shallow perturbations to a planar front.

(2) For an alloy whose composition is slightly higher than the limit point C_0^*, the shallow perturbations which are observed inside the unstable region disappear with decreasing or increasing growth velocity. These results indicate that the experiments were performed close to the "stability nose".

(3) Within the uncertainty of the material properties and the thermal gradient, the appearance of a planar front correlates well with linear stability theory. The size of the shallow cells corresponds to the theoretical results for the critical wavelength for the onset of instability.

(4) Substantial feeding flow in the remaining liquid inside the capillaries is predicted. The influence on the appearance of stability is not evaluated quantitatively. However, it is suggested that the preferred orientation of the elongated cells along the tube axis is produced by feeding flow, among other factors.

(5) The planar growth front reveals internal boundaries which look like grain boundaries. These boundaries originated from the first solid (surface dendrite) within the edges of the tubes. It is suggested that these grains are formed by recrystallization.

(6) On the basis of the experiments, it cannot be decided clearly whether the bifurcation observed is sub- or supercritical, although some indications for a supercritical bifurcation are given.

(7) No experimental evidence of oscillatory instabilities has been found. The effect of a variation of the distribution coefficient is very small for the small concentrations used. Therefore, it is probable that these instabilities do not form under the observation conditions.

Acknowledgements—The authors wish to acknowledge stimulating discussions with C. Caroli, S. H. Davis, G. Faivre, P. Metzener and M. Rappaz. Their thanks also go to J. Stramke for multiple technical assistance and his great competence in planning the experiments. This research was performed during a scholarship awarded to one of the authors (A.L.) by the Deutsche Forschungsgemeinschaft under Lu 495/1 to whom the authors wish to express their thanks.

REFERENCES

1. W. A. Tiller, K. A. Jackson, J. W. Rutter and B. Chalmers, *Acta metall.* **1,** 428 (1953).
2. W, Kurz and D. J. Fisher, *Fundamentals of Solidification*, 3rd edition. Trans Tech Aedermannsdorf, Switzerland (1989).
3. W. W. Mullins and R. F. Sekerka, *J. appl. Phys.* **35,** 444 (1964).
4. S. R. Coriell and R. F. Sekerka, *J. cryst. Growth* **61,** 499 (1983).
5. M. J. Aziz, *J. appl. Phys.* **53,** 1158 (1982).
6. W. J. Boettinger, S. R. Coriell and R. F. Sekerka, *Mater. Sci. Engng* **65,** 27 (1984).
7. W. J. Boettinger and S. R. Coriell, in *Science and Technology of the Undercooled Melt* (edited by P. R. Sahm, H. Jones and C. M. Adam), p. 81. Martinus Nijhoff, Dordrecht (1986).
8. J. C. Baker and J. W. Cahn, in *Solidification*, p. 23. ASM, Metals Park, OH (1971).
9. G. J. Merchant and S. H. Davis, *Phys. Rev. B* **40,** 11 140 (1989).
10. R. J. Braun and S. H. Davis, *J. cryst. Growth* **112,** 670 (1991).
11. G. J. Merchant, R. J. Braun, K. Brattkus and S. H. Davis, *SIAM J. appl. Math.* **52,** 1279 (1992).
12. D. A. Huntley and S. H. Davis, *Acta metall. mater.* **41,** 2025 (1993).
13. A. Karma and A. Sarkissian, *Phys. Rev. Lett.* **68,** 2616 (1992).
14. A. Karma and A. Sarkissian, *Phys. Rev. E* **47,** 513 (1993).
15. W. Kurz and R. Trivedi, *Metall. Trans.*, to be published.
16. K. A. Jackson and J. D. Hunt, *Acta metall.* **13,** 1212 (1965).
17. R. Trivedi, J. A. Sekhar and V. Seetharaman, *Metall. Trans. A* **20,** 769 (1989).
18. M. A. Chopra, Ph.D. Thesis, Rensselaer Polytechnic Institute, Troy, New York (1984).
19. M. A. Chopra, M. E. Glicksman and N. B. Singh, *Metall. Trans. A* **19,** 3087 (1988).
20. H. Esaka, Sc.D. Thesis, EPFL Lausanne (1986).
20a. A. Ludwig, internal report, EPFL, (1994).
21. R. Trivedi and W. Kurz, *Acta metall.* **34,** 1663 (1986).
22. P. W. Voorhees, S. R. Coriell, G. B. McFadden and R. F. Sekerka, *J. cryst. Growth* **67,** 425 (1984).
23. L. H. Ungar and R. A. Brown, *Phys. Rev. B* **30,** 3993 (1984).
24. S. H. Davis, in *Handbook of Crystal Growth*, Vol. 1B, (edited by D. T. J. Hurle), p. 861. Elsevier Science Publishers, Holland (1993).
25. S. R. Coriell, G. B. McFadden, R. F. Boisvert and R. F. Sekerka, *J. cryst. Growth* **69,** 15 (1984).
26. S. A. Forth and A. A. Wheeler, *J. Fluid Mech.* **188,** 202 (1989).
27. A. K. Hobbs and P. Metzener, *J. cryst. Growth* **112,** 539 (1991).
28. A. K. Hobbs and P. Metzener, *J. cryst. Growth* **118,** 319 (1992).
29. P. Metzener, private communication (1994).

30. M. E. Glicksman, R. J. Schaefer and J. D. Ayers, *Metall. Trans. A* **7,** 1747 (1976).
31. C. A. Wulff and E. F. Westrum, *J. Phys. Chem.* **67,** 2376 (1963).
32. M. E. Glicksman, J. D. Ayers and R. J. Schaefer, unpublished research, NRL (1975), cited in Ref. 30.
33. R. J. Schaefer, M. E. Glicksman and J. D. Ayers, *Phil. Mag.* **32,** 725 (1975).
34. H. C. Longuet-Higgins and J. A. Pope, *J. Chem. Phys.* **25,** 884 (1956).

APPENDIX A

Non-equilibrium Stability Analysis

The characteristic equation that determines the eigenvalues of the complex growth rate σ of an infinitesimal perturbation at a planar solid–liquid interface, including non-equilibrium conditions at the interface, has been given by Huntley and Davis [12] in their equation (4.2). Dividing by $(nR_S + R_L)(R + \bar{k} - 1)$ and rearranging gives the following equation for the steady cellular modes $[\mathrm{Re}(\sigma) = \mathrm{Im}(\sigma) = 0]$

$$\Gamma_{HD}a^2 + \frac{\tilde{G}_L}{M}\left(1 - \frac{nR_S + \mathscr{D}_L}{nR_S + R_L}\right) + \frac{\tilde{G}_S}{M}\left(n\frac{R_S + \mathscr{D}_S}{nR_S + R_L}\right)$$

$$+ \frac{\bar{m}(I)k}{k+\beta}\left(\frac{k+\beta}{1+\beta}\frac{1}{R+\bar{k}-1} - 1\right) = 0. \quad \text{(A1)}$$

As Γ is used for the Gibbs–Thomson coefficient in the present paper, Γ of Huntley and Davis is replaced by Γ_{HD}. We refer to the original paper for the definition of the symbols.

Inserting the definitions of the dimensionless quantities Γ_{HD}, $\tilde{G}_L$, $\tilde{G}_S$, M and multiplying equation (A1) by mG_C gives, with the notations used in this paper

$$\omega^2\Gamma + [\bar{\kappa}_L G_L \hat{\xi}_L + \bar{\kappa}_S G_S \hat{\xi}_S] - m_V G_C \hat{\xi}_C = 0 \quad \text{(A2)}$$

where

$$m_V = m \cdot \bar{m}(I)$$

$$\hat{\xi}_L = \bar{\kappa}_L^{-1}\left(1 - \frac{nR_S + \mathscr{D}_L}{nR_S + R_L}\right)$$

$$\hat{\xi}_S = \bar{\kappa}_S^{-1}\left(n\frac{R_S + \mathscr{D}_S}{nR_S + R_L}\right)$$

$$\hat{\xi}_C = \frac{k}{k+\beta}\left(1 - \frac{\bar{k}}{R + \bar{k} - 1}\right).$$

Considering the fact that, for the steady cellular modes, R_L, R_S, R of Huntley and Davis are the dimensionless equivalents to ω_L, ω_S, ω_C of Trivedi and Kurz [21] (the ωs multiplied by D/V), $\hat{\xi}_L$ and $\hat{\xi}_S$ are equal to the stability functions ξ_L and ξ_S in Ref. [21]. For $\hat{\xi}_C$ the following relation has to be considered

$$\hat{\xi}_C = \frac{k}{k + V/V_D}\xi_C \quad \text{(A3)}$$

where k has to be replaced by k_V in the stability function ξ_C, V_D is the diffusion velocity of the solute across the solid–liquid interface [see equation (B1)].

Thus the result of the stability analysis of Huntley and Davis [12], taking into account non-equilibrium effects at the solid–liquid interface, corresponds closely to the general stability criterion of Trivedi and Kurz (TK) developed for local equilibrium conditions [21]. The TK model can be used under non-equilibrium conditions when the equilibrium values of the distribution coefficient, k, and the liquidus slope, m, are replaced by their velocity dependent counterparts (k_V and m_V) and the stability function ξ_C is replaced by $\hat{\xi}_C$ from equation (A3).

APPENDIX B

Material Properties

Properties of pure SCN at the melting point

melting point	T_f	58.09°C	[30]
latent heat of fusion	Δh_f	4.769×10^7 J/m³	[31]
entropy of fusion	Δs_f	1.440×10^5 J/m³/K	
thermal conductivity of liquid	κ_l	0.2227 W/m/K	[32]
thermal conductivity of solid	κ_S	0.2244 W/m/K	[32]
thermal diffusivity of liquid	a_l	1.16×10^{-7} m²/s	[32]
thermal diffusivity of solid	a_S	1.14×10^{-7} m²/s	[32]
heat capacity of liquid	c_l	1.920×10^6 J/m³/K	
heat capacity of solid	c_S	1.968×10^6 J/m³K	
solid–liquid interface energy	σ	8.96×10^{-3} J/m²	[33]
Gibbs–Thomson-coefficient	Γ	6.22×10^{-8} Km	
density of liquid	ρ_l	0.970×10^3 kg/m³	[31]
density of solid	ρ_S	1.016×10^3 kg/m³	[31]
molecular weight	M	8.0092×10^{-2} kg/mol	
molar volume of liquid	v_S	7.883×10^{-5} m³/mol	
solid–liquid interface thickness	a_0	15.3×10^{-10} m	

Properties of the SCN–Ar system

liquidus slope	m	−4.7 K/wt.%	[18, 19]
equilibrium distribution coefficient	k	0.2	[18, 19]
diffusion coefficient in the liquid	D	8.8×10^{-10} m²/s	[18]
molecular weight (Ar)	M	3.9948×10^{-2} kg/mol	

Remarks

Chopra *et al.* [18, 19] determined the liquidus and solidus temperature for the SCN–Ar system as a function of the argon partial pressure. The following equation was used to transform the partial pressure into mole fraction:

$$X_L \cong \exp\left[\frac{\Delta s_f v_{ml}(T_f - T)}{RT}\right] - 1,$$

where $T_L = T_L(\Delta P)$ measured by Chopra was inserted for T to achieve a ΔP–T–X_L transformation.

Following the work of Chopra [18, 19], the liquidus slope m and the equilibrium distribution coefficient k were assumed to be constant up to 0.03 wt.%. Chopra *et al.* estimated the SCN–Ar phase diagram by determining T_L and T_S under a microscope. The temperature, at which, according to these authors, "the network of molten grain edges began to extend slowly onto the grain faces" was taken as T_S. Due to an increased amount of impurity at the grain boundaries this temperature might be too low. Thus the equilibrium distribution coefficient $k = 0.2$ estimated from this phase diagram has to be regarded as the lower limit.

The diffusion coefficient D for Ar in liquid SCN has also been evaluated by Chopra [18] where five different theoretical models were compared. Due to the best correlation between prediction and experimental results for the diffusion of gases other than Ar in different organic liquids, the model of Longuet-Higgins and Pope [34] was favoured. This model lead to $D = 8.80 \times 10^{-10}$ m^2/s. The other models gave a smaller D value. The smallest value was estimated to be $D = 5.31 \times 10^{-10}$ m^2/s.

To consider the variation of k with velocity, assumptions for the diffusion velocity of argon across the solid–liquid interface have to be made. An interface diffusion coefficient equal to the bulk diffusion coefficient in the liquid was used in the following analysis. The interface itself is assumed to expand over three molecular layers. A layer thickness is estimated by the average distance of the SCN-molecules in the solid at the melting point. Thus, the diffusion velocity across the interface is approximated by

$$V_D = \frac{D}{a_0} = \frac{D}{3}\left(\sqrt[3]{\frac{M}{\rho_S N_A}}\right)^{-1} \tag{B1}$$

where M is the molecular weight, ρ_S is the density of the solid at the melting point and N_A the Avogadro number. The resulting value for a_0 is 1.53 nm.